

Resolving the Vela C ridge with P-ArTéMiS[★] and *Herschel*^{★★}

T. Hill¹, Ph. André¹, D. Arzoumanian¹, F. Motte¹, V. Minier¹, A. Men'shchikov¹, P. Didelon¹, M. Hennemann¹, V. Könyves^{1,2}, Q. Nguyễn-Lương³, P. Palmeirim¹, N. Peretto¹, N. Schneider^{1,4,5}, S. Bontemps^{4,5}, F. Louvet¹, D. Elia⁶, T. Giannini⁶, and V. Revéret¹, J. Le Penec¹, L. Rodriguez¹, O. Boulade¹, E. Doumayrou¹, D. Dubreuil¹, P. Gallais¹, M. Lortholary¹, J. Martignac¹, M. Talvard¹, C. De Breuck⁷

(Affiliations can be found after the references)

October 2012

ABSTRACT

We present APEX/P-ArTéMiS 450 μm continuum observations of RCW 36 and the adjacent ridge, a high-mass high-column density filamentary structure at the centre of the Vela C molecular cloud. These observations, at higher resolution than *Herschel*'s SPIRE camera, reveal clear fragmentation of the central star-forming ridge. Combined with PACS far-infrared and SPIRE sub-millimetre observations from the *Herschel* HOBYS project we build a high resolution column density map of the region mapped with P-ArTéMiS. We extract the radial density profile of the Vela C ridge which with a ~ 0.1 pc central width is consistent with that measured for low-mass star-forming filaments in the *Herschel* Gould Belt survey. Direct comparison with Serpens South, of the Gould Belt Aquila complex, reveals many similarities between the two regions. Despite likely different formation mechanisms and histories, the Vela C ridge and Serpens South filament share common characteristics, including their filament central widths.

Key words. ISM: individual objects (Vela C, RCW 36) – ISM: filaments – submillimetre – ISM: dust, extinction – Stars: early-type – Stars: protostars

1. Introduction

Independent of mass, the formation of a star is a key astrophysical process: while high-mass stars drive galactic formation and ecology, low-mass stars populate their host galaxy and are themselves likely hosts of planetary systems. Although the formation paradigm for low-mass stars has been relatively well established the formation scenario for high mass stars is less clear, as are the processes involved in their formation (McKee & Ostriker 2007; Zinnecker & Yorke 2007).

The *Herschel* Space Observatory (Pilbratt et al. 2010) is providing important observational insights into both low- and high-mass star formation in our Galaxy. In particular, two *Herschel* key projects focus on low- and high-mass star formation in relatively nearby star-forming complexes: the Gould Belt survey (HGBS, 130–500 pc; André et al. 2010) and HOBYS (700 pc – 3 kpc; Motte et al. 2010), respectively. Combining these two key projects will help to examine the difference between low- and high-mass star formation.

Herschel observations in the far-infrared and submillimetre, the crucial regime for studying the birthplaces of stars, have revealed most star-forming complexes in our Galaxy to be comprised of filamentary structures (André et al. 2010; Molinari et al. 2010). Star formation proceeds in the densest (“supercritical”) of these filaments, which can be clustered into disorganised networks (nests) or into single dominating ridges (Hill et al. 2011). Arzoumanian et al. (2011) found that in

low-mass star-forming regions these interstellar filaments could be characterised by a standard central width, or thickness, of ~ 0.1 pc.

The Vela C molecular cloud was recently observed with *Herschel* as part of the HOBYS project (Hill et al. 2011; Giannini et al. 2012; Minier et al. 2012). Vela C is known to house low-, intermediate- and high-mass star formation (Massi et al. 2003; Netterfield et al. 2009; Hill et al. 2011) and is thought to be at an early stage in its evolution ($< 10^6$ yr). Running through the centre of Vela C is a ridge, a high-column density ($\sim 100 \text{ mag}^1$) self-gravitating filament, which houses the majority of the high-mass dense cores in the cloud (Hill et al. 2011). Adjacent to this ridge, and at roughly the centre of the Vela C molecular cloud is the RCW 36 ionising star cluster. Minier et al. (2012) showed that the ridge results from the ionisation of an initial sheet of molecular gas. Located at 700 pc, Vela C is the closest complex in the HOBYS sample, which allows direct comparison with low-mass star-forming regions, such as those targeted by the HGBS project, at comparable spatial resolution.

Here we present a study of the Vela C ridge and RCW 36 using the P-ArTéMiS camera² at 450 μm on APEX. P-ArTéMiS is used here to complement the *Herschel* SPIRE bands in the sub-millimetre (250, 350, 500 μm), at a factor 2–3 higher resolution (e.g. 11.5'' compared with 25'' at 350 μm).

2. Observations and data reduction

The RCW 36 region of Vela C was observed using the P-ArTéMiS bolometer camera (André et al. 2008; Minier et al.

[★] This publication is based on data acquired with the Atacama Pathfinder Experiment (APEX) in ESO program 083.C-0996. APEX is a collaboration between the Max-Planck-Institut für Radioastronomie, the European Southern Observatory, and the Onsala Space Observatory.

^{★★} *Herschel* is an ESA space observatory with science instruments provided by European-led Principal Investigator consortia and with important participation from NASA.

¹ Where $N_{H_2} = 0.94 A_V \times 10^{21} \text{ cm}^{-2} \text{ mag}^{-1}$ (Bohlin et al. 1978)

² P-ArTéMiS is a prototype for the larger format ArTéMiS camera soon to be installed on APEX (Talvard et al. 2010).

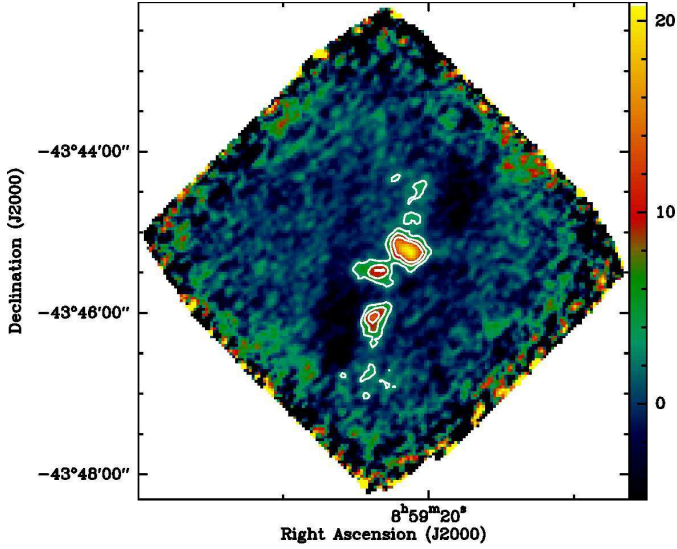


Fig. 1. P-ArTéMiS $450\ \mu\text{m}$ map of the RCW 36/Vela C ridge at $10''$ resolution. The contours are 3, 7, 11 $\text{Jy}/10''$ -beam and the rms noise level in the central part of the map is $\sim 1\ \text{Jy}/10''$ -beam.

2009) on the Atacama Pathfinder Telescope (APEX) telescope on 23 May 2009. An area of $\sim 4'$ by $4'$ was mapped in ~ 0.5 h, using a total-power, on-the-fly scanning mode. The atmospheric opacity at zenith was measured with a skydip and found to be ~ 0.8 at $\lambda = 450\ \mu\text{m}$, which corresponds to a precipitable water vapour ~ 0.7 mm. The pointing and focus of the telescope were checked using similar observing procedures to those used with APEX/LABOCA (e.g spiral scans). Flux calibration was achieved by taking spiral scans of Mars and Saturn. The pointing accuracy and absolute calibration uncertainty were estimated to be $\sim 2''$ and $\sim 30\%$, respectively. The main beam had a full width at half maximum (FWHM) $\sim 10''$, known to $\sim 10\%$ accuracy, and contained $\sim 60\%$ of the power, the rest being distributed in an “error beam” extending up to an angular radius of $\sim 80''$. The data were reduced using in-house IDL routines, following the same method as André et al. (2008) and Minier et al. (2009). This procedure includes baseline subtraction, removal of correlated sky noise and $1/f$ noise, and subtraction of uncorrelated $1/f$ noise using a method which exploits the high level of redundancy in the data. The final $450\ \mu\text{m}$ continuum map is presented in Figure 1.

The entire Vela C molecular cloud ($\sim 3\ \text{deg}^2$), including the RCW 36 region, was mapped with *Herschel* at 70, 160, 250, 350 and $500\ \mu\text{m}$ as part of the HOBYS key program. The observations and data reduction are as described by Hill et al. (2011).

3. Structural Analysis

3.1. Column density and dust temperature maps

Multiple wave-band observations covering the far-infrared and sub-millimetre regime allow construction of column density (N_{H_2}) and dust temperature maps. The maps of these quantities for the Vela C ridge/RCW 36 region, derived from *Herschel* data, were drawn using pixel-by-pixel spectral energy distribution (SED) fitting according to a modified blackbody with a single dust temperature (cf. Hill et al. 2012). Only the longest four *Herschel* wavebands were used. In order to do this, the *Herschel* observations were first convolved to the resolution of the $500\ \mu\text{m}$ band ($36''$), and the zero offsets derived from *Planck* data were

applied (see Hill et al. 2011). The quality of the SED fit was assessed using χ^2 minimisation. The corresponding column density map of the Vela C ridge and RCW 36 is given in Fig. 2 (left).

As our P-ArTéMiS data, at $10''$ resolution have better resolution than that of all of the *Herschel* SPIRE bands, we devised a method to derive a higher resolution column density map of the Vela C ridge and RCW 36 region mapped by P-ArTéMiS. By combining the PACS $160\ \mu\text{m}$, SPIRE $250\ \mu\text{m}$ and P-ArTéMiS $450\ \mu\text{m}$ data we were able to derive a column density map at $11.5''$ resolution, i.e. the resolution of the $160\ \mu\text{m}$ *Herschel* map. This method is similar to the one used by Palmeirim et al. (2012, submitted) for their higher resolution *Herschel* column density map of the Taurus B211 region, but adapted for P-ArTéMiS data as outlined in Appendix A. Due to the area covered by our P-ArTéMiS observations, only $\sim 1/3$ of the full Vela C ridge detected by *Herschel* is measured in the higher resolution column density map, which shows clear fragmentation into a number of cores/clumps. These cores are clearly visible with P-ArTéMiS (see Fig. 1) but could not be previously identified from the lower resolution *Herschel* column density map (Fig. 2, left).

3.2. Filamentary structure

At the $36''$ resolution of the *Herschel* column density map, the RCW 36 region is characterised by a single dominating high-column density filament containing the Vela C ridge (see Fig. 2). The filamentary structure seen in our higher resolution column density map is consistent with that seen in the lower resolution map, with slight deviations as it traces the topological structure of the fragmented cores (see Fig. 2, right). The mean column density of the Vela C ridge, as measured from the higher resolution column density map, is $\sim 9 \times 10^{22}\ \text{cm}^{-2}$.

The mean radial density profile (ρ_p) of the Vela C ridge (Fig. 3) was derived by measuring cuts perpendicular to the crest of the filament at each pixel, and then averaging along the length of the filament (as detailed in Arzoumanian et al. 2011). In order to derive the characteristic parameters of the profile (e.g. central density, power law exponent), we assume a cylindrical filament model given by a Plummer-like function, which is a density profile that can be expressed in terms of column density. Accordingly,

$$\rho_p(r) = \frac{\rho_c}{[1 + (r/R_{flat})^2]^{p/2}} \quad (1)$$

where ρ_c is the radial density at the centre of the filament, p is the exponent of the model function, and R_{flat} is the characteristic radius for the flat inner portion of the profile.

The Vela C ridge can be characterised by an inner radius $R_{flat} \sim 0.05 \pm 0.02\ \text{pc}$, and a deconvolved FWHM of $0.12 \pm 0.02\ \text{pc}$ which is consistent with that seen in low-mass star-forming filaments (Arzoumanian et al. 2011). The Vela C radial density profile decreases at large radii as $r^{-(2.7 \pm 0.2)}$. The filament outer radius $\sim 0.4 \pm 0.1\ \text{pc}$ is defined from the deviation of the observed (western side) profile from the Plummer fit (cf. Fig. 3). The eastern side of the profile, containing the OB star cluster, decreases up to a larger radius $\sim 1 - 1.5\ \text{pc}$ (see Fig. 4).

The radial profiles of the column density can also be used to derive a mass per unit length ($M_{line} = \int \Sigma_{obs}(r) dr$) value for a filament, by integrating the column density over the radius (cf. Arzoumanian et al. 2011). The Vela C ridge is well defined and constrained allowing us to estimate, without confusion, its mass per unit length as $M_{line} \sim 320 (\pm 75)$ or $400 (\pm 85)\ M_{\odot}/\text{pc}$ as mea-

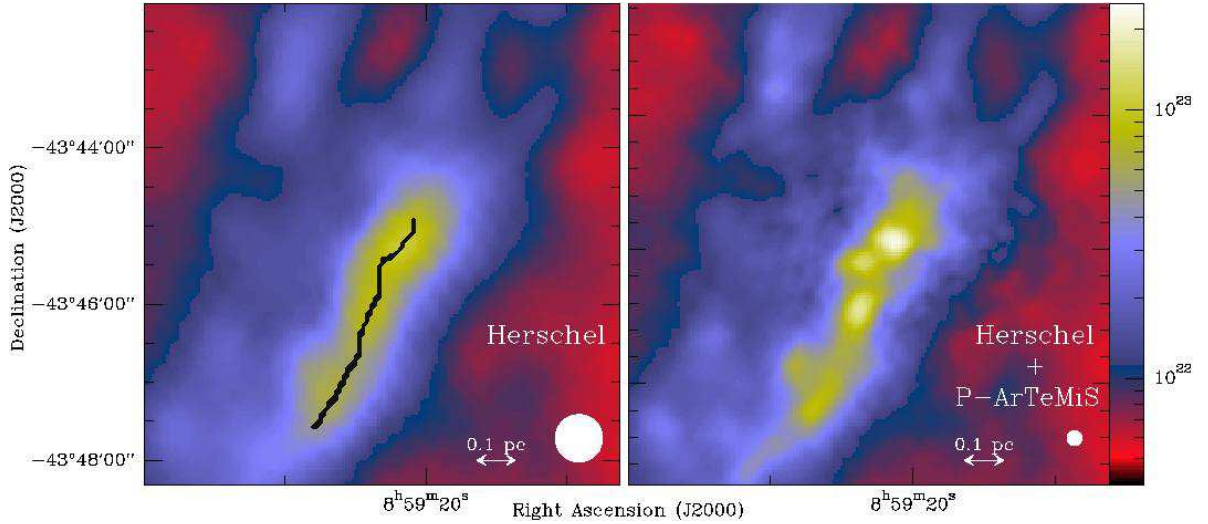


Fig. 2. The Vela C ridge/RCW 36 column density maps. The units are in $\text{H}_2 \text{ cm}^{-2}$. Left: Map derived from the longest four *Herschel* wavebands with a resolution of $36''$, equivalent to that of the SPIRE $500 \mu\text{m}$ band. Right: Map constructed using P-ArTéMiS and *Herschel* data, with resolution $11.5''$. Appendix A details how this map was created. The filament from which the radial density profile (Fig. 3) was determined (see Section 3.2) is as indicated by the black line, measured on the right map but, overlaid on the left figure for clarity.

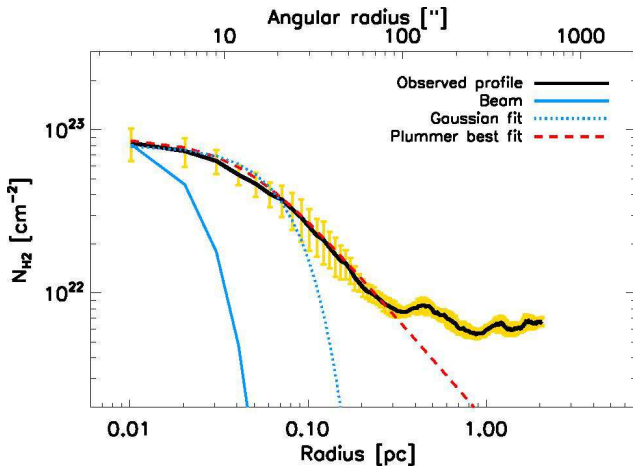


Fig. 3. The mean radial density profile (western component) perpendicular to the Vela C ridge (black line on Fig. 2, left), shown here in log-log format. The complementary eastern profile (in the direction of the star cluster) is given in Fig. 4. The area in yellow shows the dispersion of the radial profile along the filament. The solid blue line corresponds to the effective $11.5''$ HPBW resolution of the column density map (0.04 pc at 700 pc) used to construct the profile. The dotted blue line indicates the Gaussian profile, while the dotted red line shows the best fit to the model, often called the Plummer profile.

sured from the integrated radial profile of 0.4 and 1.5 pc , respectively, after subtracting a background of $3.6 \times 10^{21} \text{ cm}^{-2}$.

4. Comparison with the Serpens South filament

Recent *Herschel* observations have revealed the prolificity of interstellar filaments in star-forming complexes, though only those filaments above an A_V of ~ 8 mag are supercritical and capable of forming stars (André et al. 2010, 2011). Arzoumanian et al. (2011) showed that the filaments in low-mass HGBS regions

tend to have inner widths of $\sim 0.1 \text{ pc}$. With higher resolution P-ArTéMiS data at hand it is possible to check the application of such a characteristic filament width to more distant, higher mass regions, such as the Vela C complex at $d \sim 700 \text{ pc}$. Here we have shown that, based on its radial column density profile, the Vela C ridge has a filament inner width consistent with the characteristic inner width suggested by Arzoumanian et al. (2011). We have extended our study of filamentary structures to the Serpens South filament, part of the Aquila star-forming complex at $d \sim 260 \text{ pc}$ (see Fig. 5). The Serpens South filament is particularly interesting as it, as one of the most extreme column density filaments of the HGBS, is comprised of high-column density material, similarly to Vela C. Bontemps et al. (2010) detected seven Class 0 protostars, confirming that Serpens South is undergoing low- to intermediate-mass star formation, while Maury et al. (2011) used evolutionary tracks to estimate the lifetime of these Class-0 protostars and showed that Serpens South is at a very early phase of forming stars.

The column density map of Serpens South has been derived in the same manner as that of Vela C (see section 3.1 and Könyves et al. 2010), with only the longest four *Herschel* bands. The $36''$ resolution of this map, at the distance of Serpens South, corresponds to a spatial resolution of 0.05 pc on the sky, comparable to that of Vela C when using our higher-resolution column density maps with P-ArTéMiS data (0.04 pc at 700 pc). These two regions - Serpens South, forming low- to intermediate-mass stars, and Vela C forming intermediate and potentially high-mass stars - provide a good comparative opportunity.

The crest shown in Fig. 5 (left) for the Serpens South filament is $\sim 1.2 \text{ pc}$ in length and has an average column density value of $6.4 \times 10^{22} \text{ cm}^{-2}$ (after subtracting a background of $3.7 \times 10^{21} \text{ cm}^{-2}$). The crest shown in Fig. 2 for the Vela C ridge is $\sim 0.8 \text{ pc}$ in length and is slightly more dense at $8.6 \times 10^{22} \text{ cm}^{-2}$. The Vela C ridge and Serpens South filament have a similar mass per unit length ($M_{\text{line}} = 320$ and $290 M_{\odot}/\text{pc}$, respectively) and a similar outer radius ($\sim 0.4 \text{ pc}$; though the outer radius for both regions may be as large as $\sim 1 - 1.5 \text{ pc}$, see Figs. 4 and 5). The radial density profile of the Serpens South filament (Fig. 5)

has a (deconvolved) Gaussian FWHM width of 0.10 ± 0.05 pc, in agreement with that found here for Vela C and the characteristic width of other nearby interstellar filaments measured by Arzoumanian et al. (2011) using HGBS data. The inner width values measured for the Vela C ridge and Serpens South filament remain almost unchanged after removing the cores within them: the deconvolved FWHM values become 0.11 ± 0.01 pc and 0.14 ± 0.01 pc, respectively. As such, the common inner width of ~ 0.1 pc found in both cases may not be attributed to core properties.

The total length and mass of the Serpens South filament are of the order 2 pc and $500 M_{\odot}$, respectively, while the total length and mass of the Vela C ridge are ~ 4 pc and $\sim 600 M_{\odot}$. It should also be noted that Vela C is more distant than Serpens South, and thus core surveys in Vela C are intrinsically biased toward more massive objects than those accessible in Serpens South.

5. Universality of star-forming filament profiles?

Star formation requires a reservoir of material, concentrated into a small volume, from which the burgeoning young star can accumulate mass. The idea of a minimum mass, or density requirement, for star formation inside molecular clouds is then not surprising. Evans (2008) suggested that star formation is restricted to dense gas within molecular clouds, which also has a higher star formation efficiency than lower density gas. Comparing *Spitzer* inventories of young stellar objects with dust extinction (A_V) maps of nearby molecular clouds, both Lada et al. (2010) and Heiderman et al. (2010) suggested that star formation requires a minimum gas density (corresponding to $A_V \approx 8$ mag). Essentially the same column density threshold was recently found by André et al. (2010, 2011) from an analysis of the prestellar core population in the Aquila complex based on *Herschel* data (see also Section 1).

In addition to a minimum mass/density for core and star formation, a minimum threshold for high-mass star formation has also been suggested both theoretically (Krumholz & McKee 2008) and observationally (Kauffmann & Pillai 2010). According to these authors, low- and high-mass stars likely do not form in the same environments, with the latter requiring a minimum density, and the two modes of star formation (low- and high-mass) are distinct from each other.

In this letter we have compared two nearby (< 700 pc) regions undergoing clustered star formation. The Vela C molecular cloud is known as a low- to intermediate-mass star-forming molecular cloud. The Vela C ridge however is associated with a high-mass ionising star cluster (Minier et al. 2012), and hosts seven high-mass dense cores (Hill et al. 2011) each with the potential to form high-mass stars. Ridges are the extreme density filaments of high-mass star-forming regions whose large areas of influence suggest that they may have been formed through dynamic scenarios such as converging flows, filament mergers and/or ionisation pressure from nearby star clusters (Hill et al. 2011; Nguyen Luong et al. 2011; Hennemann et al. 2012; Minier et al. 2012). Comparatively, the Serpens South filament is populated by low- to intermediate-mass protostars (Gutermuth et al. 2008; Maury et al. 2011). Both of these filamentary star-forming clumps have supercritical masses per unit length and are thus likely to form more stars in the future.

Our analysis of the filamentary structure in the Vela C ridge and the Serpens South filament indicates that the two are quite similar with respect to their column density profile and mass per unit length, yet the Vela C ridge is a factor of ~ 2 longer and is slightly more massive than the Serpens South filament (see

Sect. 4). The lack of known Class-0 protostars in Vela C may arise from sensitivity limitations, but the same can not be said for the lack of high-mass dense cores in Serpens South.

While the Vela C ridge and Serpens South filament are likely to have formed in different environments, under different conditions, and to have experienced different histories (with, e.g., the strong ionizing effect of a massive star cluster in the case of Vela C, and no such effect in Serpens South), these two regions display a similar filament inner width ~ 0.1 pc which is also consistent with the characteristic inner width found for low-mass star-forming filaments by Arzoumanian et al. (2011). This suggests that supercritical filaments and ridges, regardless of their formation process, have the same inner width which may be characteristic across modes of star formation. These results advocate a high degree of commonality among star-forming filaments, independently of the masses of the stars they form, rather than the aforementioned idea of distinct environmental conditions for higher mass stars.

More work would be needed to establish the universality of star-forming filament profiles in the high-mass regime. Recently, Hennemann et al. (2012) used HOBYS data to show that the high-mass DR 21 ridge in the Cygnus X complex ($d \sim 1.4$ kpc) has an apparent mean central width of ~ 0.3 pc when observed at a resolution 0.17 pc. The flat inner portion of the DR 21 ridge was however only marginally resolved with *Herschel* observations. It should be stressed that higher mass star-forming ridges and filaments occur at greater distances than lower mass ones, and observations of these are thus subject to lower spatial resolution. At distances exceeding that of Vela C (> 700 pc) a characteristic inner width of ~ 0.1 pc would remain unresolved, or at best marginally resolved with *Herschel*. Higher resolution observations of high-mass star-forming filaments and ridges, with for example the full ArTéMiS camera to be installed soon on APEX or the Atacama Large Millimetre Array (ALMA), over a greater number of regions are needed now to address the hypothesis of a characteristic inner width for interstellar filaments independently of the masses of the stars they form.

Acknowledgements. T.H. is supported by a CEA/Marie-Curie Eurotalents Fellowship. Part of this work was supported by the ANR (*Agence Nationale pour la Recherche*) project ‘PROBeS’, number ANR-08-BLAN-0241.

References

- André, P., Men’shchikov, A., Bontemps, S., et al. 2010, *A&A*, 518, L102
 André, P., Men’shchikov, A., Könyves, V., & Arzoumanian, D. 2011, in *IAU Symposium*, Vol. 270, *IAU Symposium*, ed. J. Alves, B. G. Elmegreen, J. M. Girart, & V. Trimble, 255–262
 André, P., Minier, V., Gallais, P., et al. 2008, *A&A*, 490, L27
 Arzoumanian, D., André, P., Didelon, P., et al. 2011, *A&A*, 529, L6
 Bohlin, R. C., Savage, B. D., & Drake, J. F. 1978, *ApJ*, 224, 132
 Bontemps, S., André, P., Könyves, V., et al. 2010, *A&A*, 518, L85
 Evans, II, N. J. 2008, in *Astronomical Society of the Pacific Conference Series*, Vol. 390, *Pathways Through an Eclectic Universe*, ed. J. H. Knapen, T. J. Mahoney, & A. Vazdekis, 52
 Giannini, T., Elia, D., Lorenzetti, D., et al. 2012, *A&A*, 539, A156
 Gutermuth, R. A., Bourke, T. L., Allen, L. E., et al. 2008, *ApJ*, 673, L151
 Heiderman, A., Evans, II, N. J., Allen, L. E., Huard, T., & Heyer, M. 2010, *ApJ*, 723, 1019
 Hennemann, M., Motte, F., Schneider, N., et al. 2012, *A&A*, 543, L3
 Hildebrand, R. H. 1983, *QJRAS*, 24, 267
 Hill, T., Motte, F., Didelon, P., et al. 2011, *A&A*, 533, 94
 Hill, T., Motte, F., Didelon, P., et al. 2012, *A&A*, 542, A114
 Kauffmann, J. & Pillai, T. 2010, *ApJ*, 723, L7
 Könyves, V., André, P., Men’shchikov, A., et al. 2010, *A&A*, 518, L106
 Krumholz, M. R. & McKee, C. F. 2008, *Nature*, 451, 1082
 Lada, C. J., Lombardi, M., & Alves, J. F. 2010, *ApJ*, 724, 687
 Massi, F., Lorenzetti, D., & Giannini, T. 2003, *A&A*, 399, 147

- Maury, A. J., André, P., Men'shchikov, A., Könyves, V., & Bontemps, S. 2011, *A&A*, 535, A77
- McKee, C. F. & Ostriker, E. C. 2007, *ARA&A*, 45, 565
- Minier, V., André, P., Bergman, P., et al. 2009, *A&A*, 501, L1
- Minier, V., Tremblin, P., Hill, T., et al. 2012, *A&A*, submitted
- Molinari, S., Swinyard, B., Bally, J., et al. 2010, *A&A*, 518, L100
- Motte, F., Zavagno, A., Bontemps, S., et al. 2010, *A&A*, 518, L77
- Netterfield, C. B., Ade, P. A. R., Bock, J. J., et al. 2009, *ApJ*, 707, 1824
- Nguyen Luong, Q., Motte, F., Hennemann, M., et al. 2011, *A&A*, 535, A76
- Palmeirim, P., André, P., & Gould Belt consortium. 2012, submitted, *A&A*
- Pilbratt, G. L., Riedinger, J. R., Passvogel, T., et al. 2010, *A&A*, 518, L1
- Starck, J.-L. & Murtagh, F. 2006, *Astronomical Image and Data Analysis*
- Talvard, M., André, P., Le-Pennec, Y., et al. 2010, in *Society of Photo-Optical Instrumentation Engineers (SPIE) Conference Series*, Vol. 7741, Society of Photo-Optical Instrumentation Engineers (SPIE) Conference Series
- Zinnecker, H. & Yorke, H. W. 2007, *ARA&A*, 45, 481

Appendix A: Deriving a high-resolution column density map with P-ArTéMiS and *Herschel* data

The P-ArTéMiS 450 μm map (Fig. 1) provides information on small-scales in the RCW 36 ridge but is not sensitive to large-scale structures because any emission at low spatial frequencies has been completely filtered out during the process of atmospheric skynoise removal. Conversely, the *Herschel* column density map produced by Hill et al. (2011) at 36'' resolution contains little information on scales < 36'' but provides an accurate view of larger-scale features. In order to combine these two complementary data sets, we used the following procedure (inspired from Palmeirim et al. 2012, submitted).

Following the spirit of a multi-resolution data decomposition (cf. Starck & Murtagh 2006), the gas surface density distribution of the RCW 36 region, smoothed to the resolution of the *Herschel*/PACS 160 μm observations, may be expressed as a sum of four terms:

$$\Sigma_{160} = \Sigma_{500} + (\Sigma_{350} - \Sigma_{500}) + (\Sigma_{250} - \Sigma_{350}) + (\Sigma_{160} - \Sigma_{250}). \quad (\text{A.1})$$

where Σ_{500} , Σ_{350} , Σ_{250} , and Σ_{160} represent smoothed versions of the intrinsic gas surface density distribution Σ after convolution with the *Herschel* beam at 500 μm , 350 μm , 250 μm , and 160 μm respectively, i.e.: $\Sigma_{500} = \Sigma * B_{500}$, $\Sigma_{350} = \Sigma * B_{350}$, $\Sigma_{250} = \Sigma * B_{250}$, and $\Sigma_{160} = \Sigma * B_{160}$.

The first term of Eq. (A.1) is simply the surface density distribution smoothed to the resolution of the *Herschel*/SPIRE 500 μm data. An estimate, $\bar{\Sigma}_{500}$, of this term can be obtained in a manner similar to Hill et al. (2011) through pixel-by-pixel SED fitting to the longest four *Herschel* data points, assuming the following dust opacity law, very similar to that advocated by Hildebrand (1983) at submillimetre wavelengths: $\kappa_\nu = 0.1 \times (\nu/1000 \text{ GHz})^\beta = 0.1 \times (300 \mu\text{m}/\lambda)^\beta \text{ cm}^2/\text{g}$, with $\beta = 2$.

The second term of Eq. (A.1) may be written as $\Sigma_{350} - \Sigma_{500} * G_{500,350}$, where $G_{500,350}$ is a circular Gaussian with full width at half maximum (FWHM) $\sqrt{36.3^2 - 24.9^2} \approx 26.4''$. (To first order, the SPIRE beam at 500 μm is a smoothed version of the SPIRE beam at 350 μm , i.e., $B_{500} = B_{350} * G_{500,350}$.) The second term of Eq. (A.1) may thus be viewed as a term adding information on spatial scales accessible to SPIRE observations at 350 μm , but not at 500 μm . In practice, one can derive and estimate $\bar{\Sigma}_{350}$ of Σ_{350} in a manner similar to $\bar{\Sigma}_{500}$, through pixel-by-pixel SED fitting to three *Herschel* data points between 160 μm and 350 μm (i.e., ignoring the lower resolution 500 μm data point). An estimate of the second term of Eq. (A.1) can then be obtained by subtracting a smoothed version of $\bar{\Sigma}_{350}$ (i.e., $\bar{\Sigma}_{350} * G_{500,350}$) to $\bar{\Sigma}_{350}$ itself, i.e., by removing low spatial frequency information from $\bar{\Sigma}_{350}$.

Likewise, the third term of Eq. (A.1) may be written as $\Sigma_{250} - \Sigma_{250} * G_{350,250}$, where $G_{350,250}$ is a circular Gaussian with FWHM $\sqrt{24.9^2 - 18.2^2} \approx 17.0''$, and may be understood as a term adding information on spatial scales only accessible to *Herschel* observations at wavelengths $\leq 250 \mu\text{m}$. In order to derive an estimate $\bar{\Sigma}_{250}$ of Σ_{250} on the right-hand side of Eq. (A.1), we first smoothed the PACS 160 μm map to the 18.2'' resolution of the SPIRE 250 μm map and then derive a color temperature map between 160 μm and 250 μm from the observed $I_{250 \mu\text{m}}(x, y)/I_{160 \mu\text{m}}(x, y)$ intensity ratio at each pixel (x, y) . The SPIRE 250 μm map was converted to a gas surface density map ($\bar{\Sigma}_{250}$), assuming optically thin dust emission at the temperature given by the color temperature map and a dust opacity at 250 μm $\kappa_{250 \mu\text{m}} = 0.1 \times (300/250)^2 \text{ cm}^2/\text{g}$. An estimate of the third term of Eq. (A.1) can then be obtained by subtracting a smoothed version of $\bar{\Sigma}_{250}$ (i.e., $\bar{\Sigma}_{250} * G_{350,250}$) to $\bar{\Sigma}_{250}$ itself, i.e., by removing low spatial frequency information from $\bar{\Sigma}_{250}$.

The fourth term on the right-hand side of Eq. (A.1) is the component containing information on the smallest scales $\sim 10 - 18''$ and which was estimated using the P-ArTéMiS data. It may be written as $\Sigma_{160} - \Sigma_{160} * G_{250,160}$, where $G_{250,160}$ is a circular Gaussian with FWHM $\sqrt{18.2^2 - 11.5^2} \approx 14.1''$. In order to derive an estimate $\bar{\Sigma}_{160}$ of Σ_{160} on the right-hand side of Eq. (A.1), we used the color temperature map between 160 μm and 250 μm (18'' resolution) to convert a slightly smoothed version of the P-ArTéMiS 450 μm data (11.5'' resolution) and the PACS 160 μm data to a column density map at 11.5'' resolution, assuming optically thin dust emission and the same dust opacity law as above. Due to skynoise filtering, the latter map ($\bar{\Sigma}_{160}$) does not contain information on angular scales $\gtrsim 40''$, but this is not a problem since our estimate of the fourth term of Eq. (A.1) was obtained by subtracting a smoothed version of $\bar{\Sigma}_{160}$ (i.e., $\bar{\Sigma}_{160} * G_{250,160}$) to $\bar{\Sigma}_{160}$ itself, i.e., by removing any information on scales $\gtrsim 18''$ from $\bar{\Sigma}_{160}$. This subtraction of scales larger than $\sim 18''$ from $\bar{\Sigma}_{160}$ also suppresses the effect of the bowls of negative emission seen at $\pm 30''$ on either side of the central ridge in the P-ArTéMiS 450 μm map (Fig. 1).

Our final estimate $\bar{\Sigma}_{160}$ of the gas surface density distribution at 11.5'' resolution was produced by summing the above estimates of the four terms on the right-hand side of Eq. (A.1):

$$\begin{aligned} \bar{\Sigma}_{160} = & \bar{\Sigma}_{500} + (\bar{\Sigma}_{350} - \bar{\Sigma}_{350} * G_{500,350}) + (\bar{\Sigma}_{250} - \bar{\Sigma}_{250} * G_{350,250}) \\ & + (\bar{\Sigma}_{160} - \bar{\Sigma}_{160} * G_{250,160}). \quad (\text{A.2}) \end{aligned}$$

The resulting 11.5'' resolution column density map \tilde{N}_{H_2} for the RCW36 region is displayed in the right panel of Fig. 2 in units of mean molecules per cm^2 , where $\bar{\Sigma}_{160} = \mu m_{\text{H}_2} \tilde{N}_{\text{H}_2}$ and $\mu = 2.33$ is the mean molecular weight. This high-resolution column density map is subject to larger uncertainties than the standard 36.3''-resolution column density map derived from *Herschel* data. In particular, the absolute calibration uncertainty of the ground-based P-ArTéMiS 450 μm data is larger ($\sim 30\%$) than that of the *Herschel* data ($\lesssim 10\%$), and the beam shape of the P-ArTéMiS instrument is also more uncertain³ than the beams of the SPIRE and PACS cameras on *Herschel*. To test the reliability and robustness of this 11.5'' resolution column density map, we smoothed it to the 36.3'' resolution of the standard column density map (corresponding to $\bar{\Sigma}_{500}$) and inspected the ratio map

³ Note, however, that the $\lesssim 80''$ error beam of the P-ArTéMiS instrument is effectively filtered out during the data reduction and map reconstruction process, so that only the $\sim 10\%$ uncertainty in the $\sim 10''$ main beam of P-ArTéMiS matters here for $\bar{\Sigma}_{160}$.

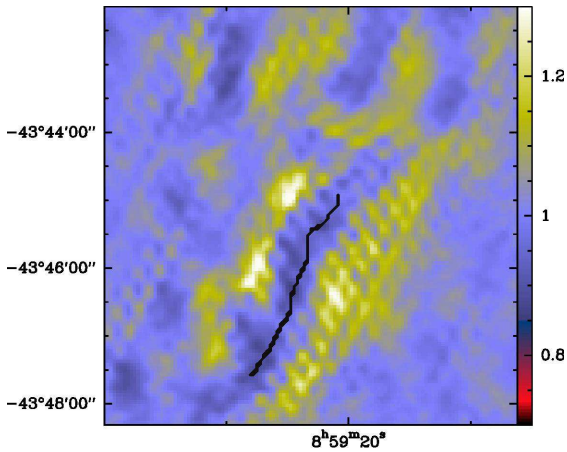


Fig. A.1. Ratio map of the 11.5'' resolution column density map (corresponding to Σ_{160}) smoothed to 36.3'' resolution divided by the standard column density map (corresponding to Σ_{500}). The same filament crest as in Fig. 2 is overlaid. The maximum value of the ratio is 1.35 and the minimum value is 0.85.

between the two, which has a mean value of 1.00 and a standard deviation of 0.03 (see Fig. A.1). The two column density maps agree to better than 35% everywhere. The morphology and amplitude of the features seen in the ratio map (Fig. A.1) suggest that the potential artefacts present in the high-resolution column density map translate into an uncertainty of $\lesssim 40\%$ in the radial column density profiles shown in Fig. 3 and Fig. 4 (left). This uncertainty is comparable to the yellow error bars shown on the profiles (corresponding to the dispersion of the radial profiles observed along the ridge) and therefore does not significantly affect our conclusions regarding the shape and central width of the radial density profile.

Finally, we note that our column density map of the Vela C ridge is also more uncertain than that of the Serpens South filament owing to the strong heating effect of the RCW36 cluster and its uncertain location along the line of sight. Simple tests suggest that this effect leads to an additional 50% uncertainty in the absolute calibration of the column density map of the Vela C ridge but has little influence on the shape of the radial column density profile.

¹ Laboratoire AIM, CEA/IRFU CNRS/INSU Université Paris Diderot, CEA-Saclay, 91191 Gif-sur-Yvette Cedex, France

² Institut d'Astrophysique Spatiale, CNRS/Université Paris-Sud 11, 91405 Orsay, France

³ Canadian Institute for Theoretical Astrophysics - CITA, University of Toronto, 60 St. George Street, Toronto, Ontario, M5S 3H8, Canada

⁴ Université de Bordeaux, Bordeaux, LAB, UMR 5804, 33270, Floirac, France

⁵ CNRS, LAB, UMR 5804, 33270, Floirac, France

⁶ IAPS- Istituto di Astrofisica e Planetologia Spaziali, via Fosso del Cavaliere 100, 00133 Roma, Italy

⁷ European Southern Observatory, Karl Schwarzschild Str. 2, 85748 Garching bei Munchen, Germany
e-mail: tracey.hill@cea.fr

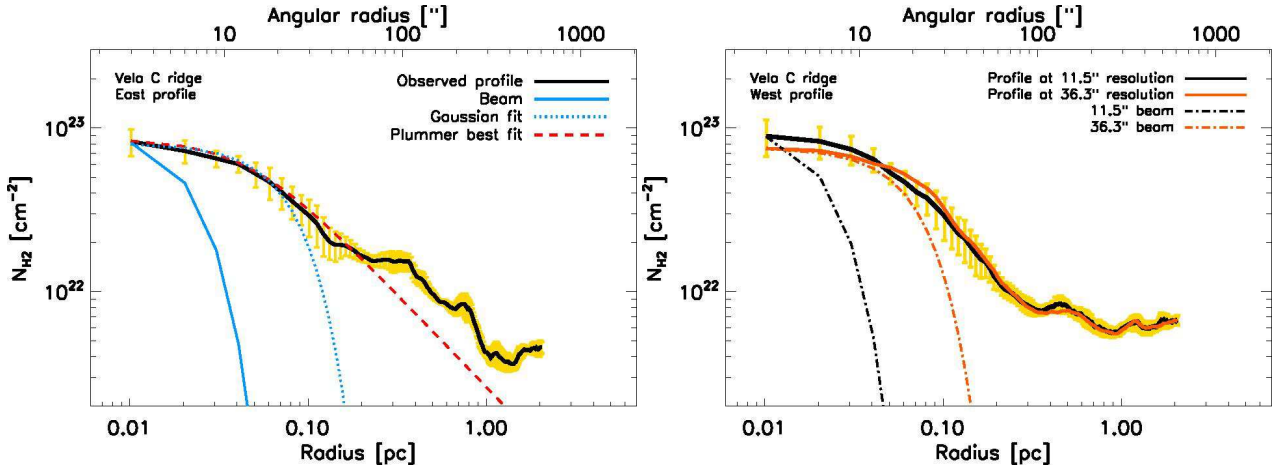


Fig. 4. Left: Mean radial column density profile measured on the eastern side of the Vela C ridge in the 11.5'' resolution column density map shown in Fig. 2 (right). This figure is complementary to Fig. 3 for the side containing the OB cluster. This profile has a p value of 2.3 ± 0.5 and $R_{flat} = 0.05 \pm 0.02$ pc. The error bars in yellow show the dispersion of the radial profile along the filament, while the lines on the plot are as per Fig. 3 and as indicated on the key. Right: Comparison of the mean background-subtracted radial profiles measured on the western side of the Vela C ridge in the 11.5'' resolution column density map (black curve and yellow error bars) and in the 36.3'' resolution column density map (orange curve). The black and orange dash-dotted curves represent the effective 11.5'' and 36.3'' HPBW resolutions of the corresponding data, respectively.

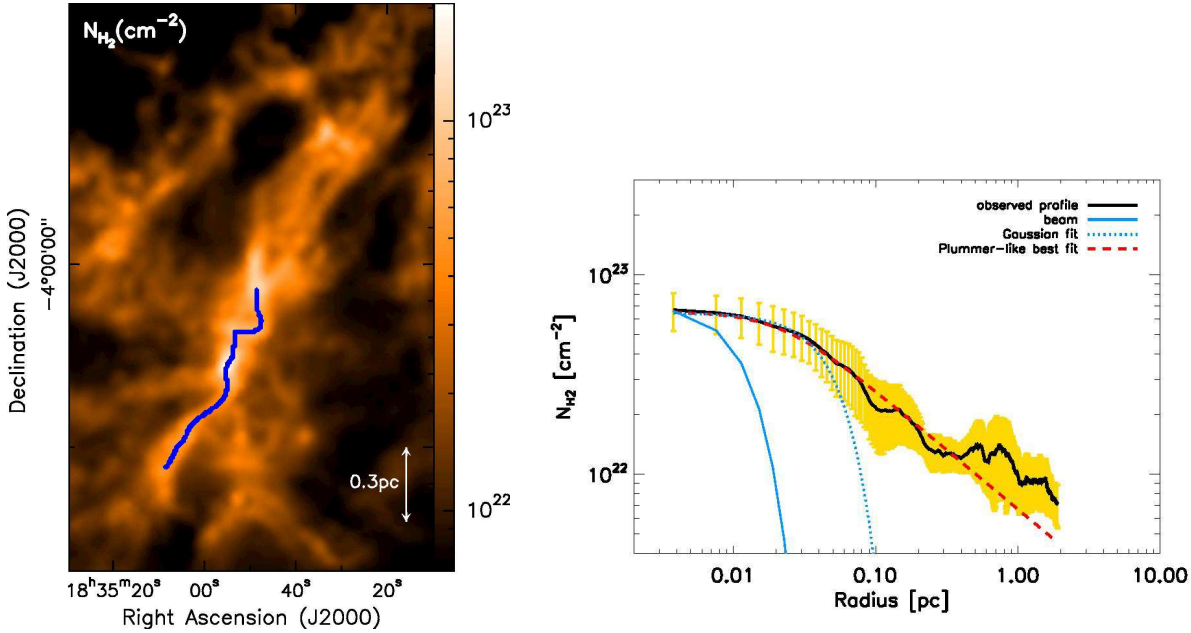


Fig. 5. Left: Column density map of the Serpens South filament (36'' resolution) derived from HGBS data (see Könyves et al. 2010), with the corresponding topological filament identified overlaid in blue. Right: Mean radial density profile (taken from both sides of the filament) measured perpendicular to the supercritical Serpens South filament (left) shown here in log-log format. Lines and colour coding are consistent with Figs. 3 and 4. The Gaussian fit to the inner part of the profile (dotted blue curve) has a deconvolved FWHM width 0.10 ± 0.05 pc. The best Plummer-like model fit (dashed red curve) has an inner radius $R_{flat} \sim 0.03 \pm 0.01$ pc and a power-law index $p = 2.02 \pm 0.27$.